

Precursory atmospheric circulations with Rossby wave trains leading to Eurasian extreme cold events

Wenqin zhuo

Ocean University of China

Fei Huang (✉ huangf@mail.ouc.edu.cn)

Ocean University of China <https://orcid.org/0000-0002-1119-9081>

Ruichang Ding

Ocean University of China

Jin Luo

Ocean University of China

Research Article

Keywords: Eurasia, extreme cold events, Rossby wave packets, downstream development

Posted Date: September 3rd, 2021

DOI: <https://doi.org/10.21203/rs.3.rs-849842/v1>

License: © ⓘ This work is licensed under a Creative Commons Attribution 4.0 International License.

[Read Full License](#)

1
2
3
4
5
6
7
8
9
10
11
12
13
14
15
16
17
18
19
20
21
22
23
24
25
26
27
28
29

**Precursory atmospheric circulations with Rossby wave trains leading
to Eurasian extreme cold events**

Wenqin Zhuo^{1,2}, Fei Huang^{*1,2,3}, Ruichang Ding^{1,2}, Jin Luo^{1,2}

Submitted on August 26 2021

¹ Key Laboratory of Physical Oceanography, Institute for Advanced Ocean Study, Ocean University of China, Qingdao, China.

² College of Oceanic and Atmospheric Sciences, Ocean University of China, Qingdao, China

³ Qingdao National Laboratory for Marine Science and Technology, Qingdao, China.

*Corresponding author: Fei Huang (huangf@ouc.edu.cn)

30 **Abstract**

31 This work examines precursory atmospheric circulations with various wave trains contributing to
32 extreme cooling over central Eurasia in boreal winter from 1979-2016 based on the ERA-Interim dataset.
33 The empirical orthogonal function (EOF) method is used to classify the anomalous sea level pressure
34 field averaged in two weeks prior to extreme cooling. Based on the classification, three types of
35 precursory atmospheric circulation patterns are named according to the origins of wave trains, and their
36 formation mechanisms are revealed as well. Type1: Baffin Bay-origin pattern, which forms in the
37 downstream development of Rossby wave packets generated from the downward stratospheric energy
38 transmission over the Baffin Bay. Type2: Pacific-origin pattern, similar to a Eurasian (EU) teleconnection
39 pattern, arises at the exit area of the westerly jet in the central North Pacific where cyclonic shear exists;
40 then it develops along the northerly westerly jet over the North Atlantic, which may act as a waveguide
41 to the Eurasian continent. Type 3: Atlantic-origin, manifests as the negative phase of type 2, consistent
42 with the Scandinavian (SCAND) pattern, which may results from the air-sea interaction induced by the
43 warm anomaly of sea surface temperature in the middle of North Atlantic. In conclusion, the three types
44 of precursory atmospheric wave train patterns that bring extreme cooling to Eurasia possess diverse
45 disturbing sources and development mechanisms. The results, which are investigated based on a quasi-
46 biweekly time scale, deepen our understanding of the atmospheric genesis of extreme weather and have
47 specific indicative significance to improve the technique of extended forecast.

48 **Keywords:** Eurasia, extreme cold events, Rossby wave packets, downstream development

59 **Declarations**

60 **Funding**

61 The research is supported by National Key Scientific Research Program of China (2019YFA0607004),
62 the National Science Foundation of China (42075024) and Shandong Natural Science Foundation Project
63 (ZR2019ZD12)

64 **Conflicts of interest/Competing interests**

65 All the authors declare no conflicts of interest and competing interests

66 **Availability of data and material**

67 All the data and material are available

68 **Code availability**

69 The code is not available

70 **Ethics approval**

71 Not applicable

72 **Consent to participate**

73 All the authors consent to participate this work

74 **Consent for publication**

75 All the authors consent the work for publication

76

77

78

79

80

81

82

83

84

85

86

87

88

89 **1 Introduction**

90 Frequently extreme cooling occurred in the boreal winter over central Eurasia in recent years (Cohen
91 et al. 2012,2014; Zhang et al. 2012; Lu et al. 2016; Ma et al. 2018; Mori et al. 2019; Zheng et al.,2021).
92 The mechanisms of extreme cold climate anomalies have been widely discussed. There are many studies
93 that focus on the external compulsion factors, such as the Arctic amplification (Cohen et al. 2019), and
94 sea ice melt owing to Arctic warming (Zhuo and Jiang,2020), the stratospheric influence (Kretschmer et
95 al. 2018), the force of sea surface temperature over Atlantic (Luo et al. 2019), etc. However, the ultimate
96 impact factors of extreme weather still have to be traced back to the general atmospheric circulation, that
97 is, the propagation of Rossby waves, which transfer energy, moisture, and momentum across long
98 distances (Wallace and Gutzler 1981).

99 There are many atmospheric teleconnections that can induce significant climate anomalies over the
100 Eurasian continent. For example, the Eurasian (EU) pattern (Wallace and Gutzler,1981), which shows
101 like west–east-oriented wave train over Eurasia and can be further divided into the forms of Scandinavian
102 (SCAND) pattern and East Atlantic/West Russia pattern (Barnston and Livezey, 1987). Those various
103 patterns have distinct sources and formation mechanisms (Casado et al. 2009; Liu et al. 2014). Take the
104 SCAND pattern, which is typically generated from the North Atlantic and can be classified into
105 convection-preceded and convection-free types (Wang and Tan,2020). Besides, the North Atlantic
106 Oscillation (NAO) pattern can also exert influence on the climate over Eurasia by affect the Arctic sea
107 ice melt (Luo et al. 2016a, b). In addition to these typical teleconnection circulation patterns, the
108 atmospheric wave trains can also propagate along the strong westerly jets (Hoskins and Ambrizzi 1993),
109 which can serve as efficient Rossby waveguides (Chang and Yu 1999; Branstator, 2002). When a wave
110 train extracts energy from mean flow, it is conducive to the further progress of the Rossby wave (Kosaka
111 et al. 2009; Hu et al. 2018), and extreme weather occurred under the configuration of mature atmospheric
112 circulation.

113 Under certain circumstances, Rossby waves can propagate from upstream to downstream along with
114 the westerlies as Rossby wave packets (RWPs), which can be observed in the upper troposphere. To some
115 extent, therefore, the evolution of Rossby wave can be a precursor to extreme weather (Wirth and
116 Eichhorn,2014; Bosart et al. 2017; Wirth et al. 2018; Fragkoulidis et al. 2018; Grazzini et al. 2020). For
117 example, Wirth and Eichhorn (2014) examined the statistical connection between surface cyclones over

118 Europe and Rossby wave trains in the upper-troposphere, then concluded that the occurrence of upstream
119 RWPs significantly increases the probability of downstream cyclone development. Grazzini et al. (2020)
120 pointed out that the amplification of RWPs over the western North Atlantic can result in a downstream
121 trough, which is highly related to the extreme precipitation events over Italy. The RWPs along the
122 westerly jet in the upper troposphere may also impact the precipitation in the Yangtze River over China
123 (Shi et al. 2009; Sun and Guan,2020). Areas of large RWP amplitude are found to be associated with an
124 increased probability of extremes temperature in lower-tropospheric (Fragkoulidis et al. 2018). However,
125 not every extreme weather event is necessarily related to an RWP precursor (Barton et al. 2016; Wirth et
126 al. 2018). The climate affects variously when the dispersion degree and range of energy differ. Under
127 certain conditions, other atmospheric signals, such as the downward propagation of AO (Gong et al.
128 2014), the anomalies of pressure extend from lower troposphere to stratosphere (Shi et al.,2021), were
129 also conducive to Rossby wave train propagation and lead to extreme weather occurs.

130 Anyway, enhanced understanding of RWPs could contribute to improving the weather forecast,
131 particularly with extreme weather conditions. Thus it is essential to examine the character of wave trains
132 that can give rise to extreme cooling, which is of great significance in probing the systematic connection
133 between precursory RWPs and severe climate and further improving the extended forecast technique. In
134 this work, we will analyze the basic features and formation mechanisms of various wave trains that lead
135 to extreme cooling over central Eurasia in winter, by selecting the extreme cold events and classifying
136 the corresponding anomalous circulations in prior to cooling.

137 The dataset and methods are described in Section 2. Section 3 classifies the circulation of cold events
138 into three types and presents corresponding circulation anomalies of each type. The characteristics and
139 mechanisms of each category's events are discussed respectively in Section 4. Conclusions and
140 discussions are presented in Section 5.

141 **2 Data and methods**

142 The daily mean ECMWF reanalysis (ERA)-Interim dataset (Dee et al. 2011) for boreal winter
143 (December-February (DJF)) from 1979–2016 are used, with a horizontal resolution of 1° latitude \times 1°
144 longitude. Variables include the 2-m surface air temperature (SAT), sea level pressure (SLP), geopotential
145 height, sea surface temperature (SST), surface turbulent heat flux (STHF (sensible plus latent)), zonal (u)
146 and meridional (v) winds. Anomalies of each variable are calculated by subtracting 1979–2016

147 climatological mean for each calendar day at each grid point.

148 To investigate the mechanisms of Eurasia cooling, 29 extreme cold events are identified over central
149 Eurasia (40°N–60°N, 60°E–120°E) where emerged a cooling trend in recent decades (Mori et al. 2019).
150 An extreme cold event is defined over a period when the domain-averaged SAT reaches the criterion of
151 the probability of occurrence less than 10% (namely, 253.49 K or –19.66°C) and persists for more than
152 3 days. Besides, to avoid the non-independent circulation system, the interval between two cold events
153 needs to exceed 15 days (Wu et al. 2017). Lag 0 for a cold event is defined as the onset day when the
154 domain-averaged SAT index first reaches its criterion, and the life cycle of each event refers to the
155 number of consecutive days that meet the standard. The detail information and corresponding
156 classification results about each case, which will further describe in next section, are listed in the Table
157 1.

158 **Table 1.** The information of onset date (yyyy-mm-dd) and life cycle (unit: days) and corresponding
159 category of each case

Number	Onset date	Life cycle	Category	Number	Onset date	Life cycle	Category
1	19800126	14	Type 1	16	20011209	4	Type 3
2	19810120	5	Type 2	17	20021228	4	Type 3
3	19840121	17	Type 2	18	20041223	6	Type 2
4	19841210	7	Type 3	19	20050123	17	Type 2
5	19861224	3	Excluded	20	20060102	3	Type 3
6	19880121	6	Type 3	21	20080110	20	Type 3
7	19880212	3	Type 2	22	20100101	3	Type 1
8	19900115	5	Type 3	23	20100202	12	Type 3
9	19911223	3	Excluded	24	20101221	3	Type 1
10	19940114	4	Type 1	25	20110115	12	Type 1
11	19960110	7	Type 3	26	20120117	17	Type 2
12	19980111	13	Type 2	27	20121212	16	Type 1
13	20000102	7	Excluded	28	20140201	5	Type 3
14	20010103	10	Type 1	29	20160117	6	Type 1
15	20010131	7	Type 3				

160 The composite calculations are conducted to investigate the evolution of atmospheric variables

161 related to cold events. For qualitative discussion, we perform Empirical Orthogonal Function (EOF)
 162 analysis to classify the atmospheric circulations. Furthermore, the wave activity flux (WAF) following
 163 Takaya and Nakamura et al. (2001), which is parallel to the local group velocity of stationary Rossby
 164 wave and can be used to describe the propagation of the atmospheric wave train, is calculated and
 165 expressed as follows:

$$166 \quad W = \frac{p \cos \varphi}{2|U|} \cdot \left(\begin{array}{c} \frac{U}{a^2 \cos^2 \varphi} \left[\left(\frac{\partial \psi'}{\partial \lambda} \right)^2 - \psi' \frac{\partial^2 \psi'}{\partial \lambda^2} \right] + \frac{V}{a^2 \cos \varphi} \left[\frac{\partial \psi'}{\partial \lambda} \frac{\partial \psi'}{\partial \varphi} - \psi' \frac{\partial^2 \psi'}{\partial \lambda \partial \varphi} \right] \\ \frac{U}{a^2 \cos \varphi} \left[\frac{\partial \psi'}{\partial \lambda} \frac{\partial \psi'}{\partial \varphi} - \psi' \frac{\partial^2 \psi'}{\partial \lambda \partial \varphi} \right] + \frac{V}{a^2} \left[\left(\frac{\partial \psi'}{\partial \varphi} \right)^2 - \psi' \frac{\partial^2 \psi'}{\partial \varphi^2} \right] \\ \frac{f_0^2}{N^2} \left\{ \frac{U}{a \cos \varphi} \left[\frac{\partial \psi'}{\partial \lambda} \frac{\partial \psi'}{\partial z} - \psi' \frac{\partial^2 \psi'}{\partial \lambda \partial z} \right] + \frac{V}{a} \left[\frac{\partial \psi'}{\partial \varphi} \frac{\partial \psi'}{\partial z} - \psi' \frac{\partial^2 \psi'}{\partial \varphi \partial z} \right] \right\} \end{array} \right)$$

167 where φ , λ , z denote latitude, longitude, vertical coordinate, respectively; a is Earth' radius, f_0 is Coriolis
 168 parameter, p is pressure, N^2 is buoyancy frequency squared; U , V denote the climatological zonal and
 169 meridional horizontal wind, and ψ' is anomaly of stream function.

170 Finally, two-tailed Student's t-test is used for statistically significant levels.

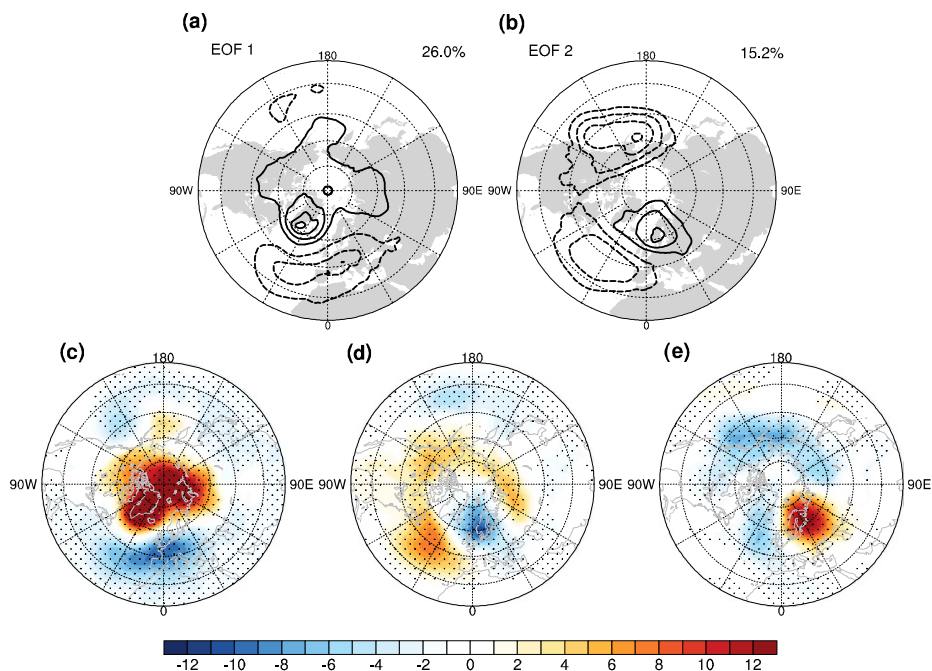
171 **3 Features of Eurasian extreme cold events and corresponding precursory atmospheric** 172 **wave train patterns**

173 **3.1 Classification of Eurasian extreme cold events**

174 Considering the fact that there are various atmospheric circulations that cause Eurasia cooling
 175 (Horton et al. 2015; Hu et al. 2018; Wang and Tan 2020), we classify the circulation systems based on
 176 atmospheric in two weeks preceding the cold event. Figure 1a-b shows two leading modes of atmospheric
 177 circulation anomalies by using the EOF analysis on the composite SLP anomalies averaged in lag from
 178 -14 to -1 days. The first mode explains 26% of the variance, where the positive SLP anomalies dominate
 179 the Arctic circle and the center of action located in the southwest of Greenland, while the negative SLP
 180 anomalies dominate the area from western Atlantic to eastern Europe, resembling the northwest-
 181 southeast negative phase of NAO. The second mode, which explains 15.2% of the variance, has a solid
 182 positive anomalous SLP center located at the Scandinavia peninsula, and the northeast Pacific to North
 183 Atlantic area are all controlled by the negative SLP anomalies.

184 According to these two leading modes of EOF analysis, 29 cold events are reclassified into three
 185 types. It should be noted that not only the PC time series (supplementary Fig. S1) but also the average
 186 SLP anomalies field of each case (Fig.S2) are referred to when categorizing the circulations, thus
 187 ensuring that the system affecting the cooling area has the greatest similarity to the EOF mode. Figure

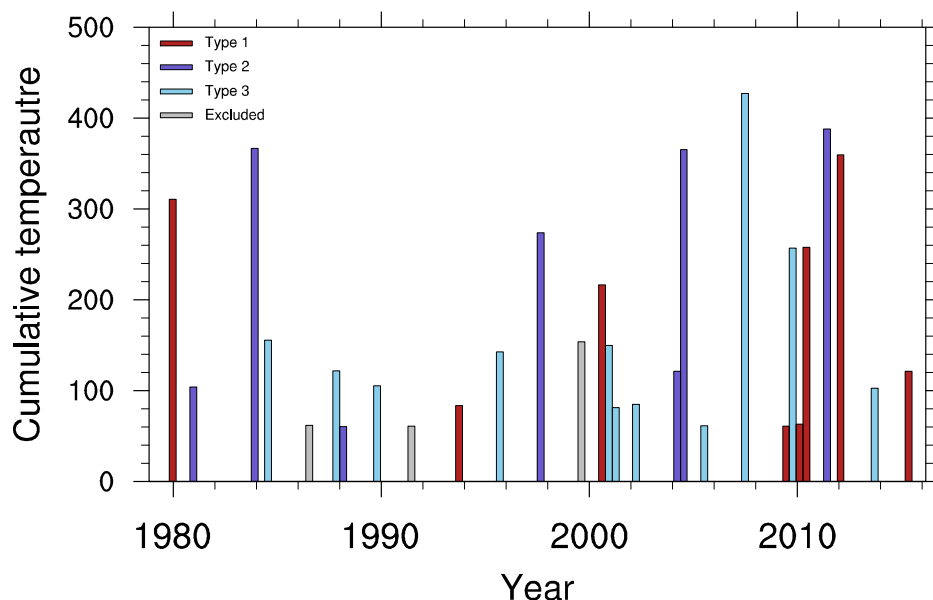
188 1c-f show the composite fields of anomalous SLP of each type after classification. The first type (type1,
 189 Fig.1c) is similar to EOF1 mode, which exhibits the northwest-southeast negative phase of NAO, with 8
 190 cases in total (Table 1). The second type (type 2, Fig.1d) like the negative phase of EOF2 mode and is
 191 similar to the EU pattern, which has one negative center of action around the Scandinavian Peninsula
 192 and two other centers of activity with opposite signs over the north Atlantic and Siberia area, consist of
 193 7 cases (Table 1). The third type (type3, Fig.1e) is close to the positive phase of EOF2 mode, shows like
 194 the SCAND pattern, which has a positive center of action located at the Scandinavian Peninsula, consist
 195 of 11 cases (Table 1). In addition, there are three cases that exhibit the negative phase of EOF1 mode
 196 (Table 1), thus they are excluded in this paper due to the small sample size. In this way, all cases are
 197 classified into three types of cold events for qualitative discussion.



198
 199
 200 **Fig. 1 a-b** Spatial patterns of two leading EOF modes of anomalous SLP averaged in lag -14 to -1 days
 201 based on 29 cold events, explaining 26 and 15.2% of total variance, respectively; **c-e** Composite fields
 202 of anomalous SLP (unit: hPa) averaged in lag -14 to -1 days of **c** type1, **d** type2, **e** type3 event. The
 203 anomalies over stippled regions in **c-e** are statistically significant above 95% confidence level according
 204 to the Student's t test

205 The distribution of the cumulative negative temperature (multiplied by -1) during each case's life
 206 cycle and the related classification is shown in Fig.2 to detect the essential characteristics of three types
 207 of events. In general, it can be seen that the cold events occurred more frequently after the winter in

208 1999/2000. This phenomenon, namely the frequent cold winter in Eurasia, has attracted many scholars'
 209 attention (Zhang et al. 2012; Kug et al. 2015; Lu et al. 2016). Specifically, it shows that the type 1 event
 210 occurs more often in the winter after 2009/2010, while type 3 takes place more frequently between
 211 1999/2000 to 2008, and the coldest case occurred in 2008. In the following, the three groups of
 212 anomalous circulations after composition are discussed separately.

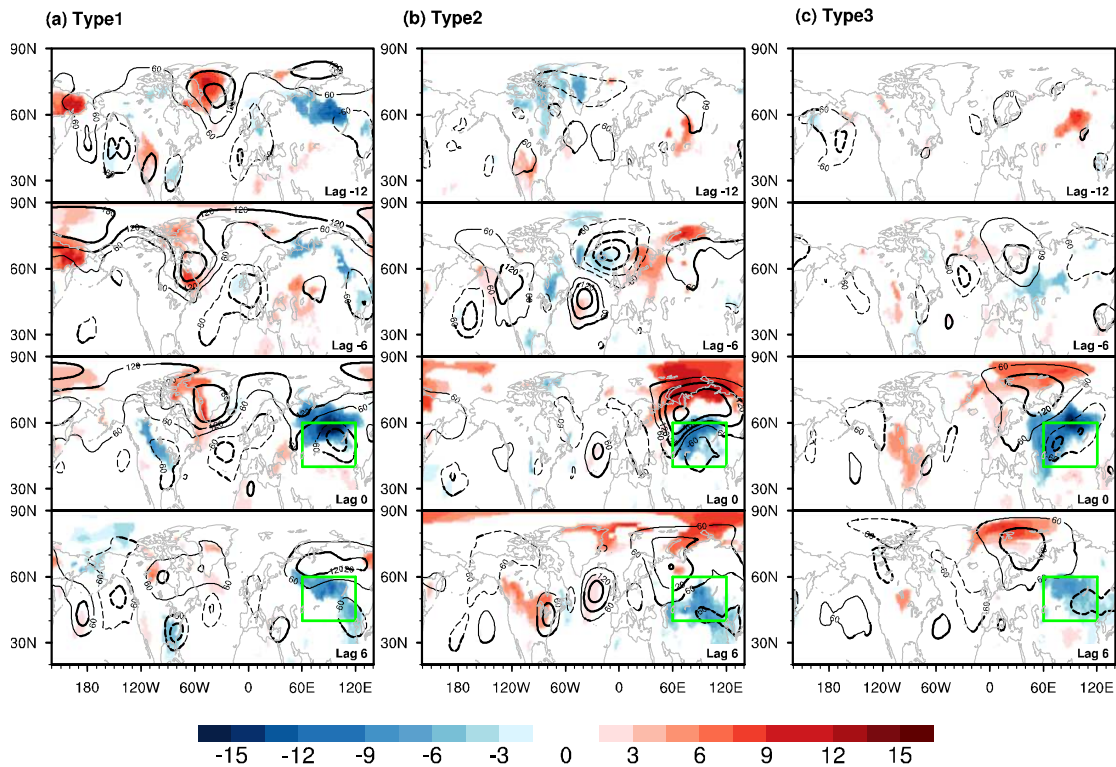


213
 214 **Fig. 2** Time series of cumulative negative temperature (multiplied by -1) of 29 cases and corresponding
 215 classification

216 3.2 Corresponding atmospheric circulation anomalies

217 Before analyzing the mechanisms of cold events, the evolution of anomalous 500-hPa geopotential
 218 height and SAT fields of three types of cold events over time is shown in Fig.3. It can be seen that the
 219 cooling situation can last for a week for all three events (lag 0-6 days in Fig.3a-c). Furthermore, for type
 220 1 event (Fig.3a), a positive anomalous action center is located around over eastern Greenland at lag -12
 221 days, as it continues to grow and strengthen, the downstream system over Eurasia also begins to evolve,
 222 and the cold anomalies appear over the north of central Eurasia at lag 0 days; After that, at lag 6 days,
 223 the upstream system over the Greenland decays, with the cold anomalies weaken and fade away. For type
 224 2 event (Fig. 3b), clearly system appears at lag -6 days, with a wave train stretching from mid-North
 225 Pacific to the European continent; then, the upstream system degrades and a solid positive anomaly center
 226 located Ural Mountain area at lag 0 days, leading the outbreak of cooling over Eurasia. For type 3 event
 227 (Fig.3c), a weak positive anomaly center over Scandinavia begin to develop since lag -12 days, with two

228 other opposite centers of action over the central Atlantic and Europe; as the anticyclone anomalies
 229 intensify, the wave train evolves into the mode like the SCAND teleconnection pattern (Barnston and
 230 Livezey, 1987) at lag 0 days and brings cold anomalies into Eurasia. In general, though there is little
 231 difference in the cooling situation of three types of events after lag 0 days, the atmospheric systems in
 232 the prophase of cold events differ greatly. Therefore, in the next section, the generation mechanisms of
 233 three kinds of cold events will be examined respectively.



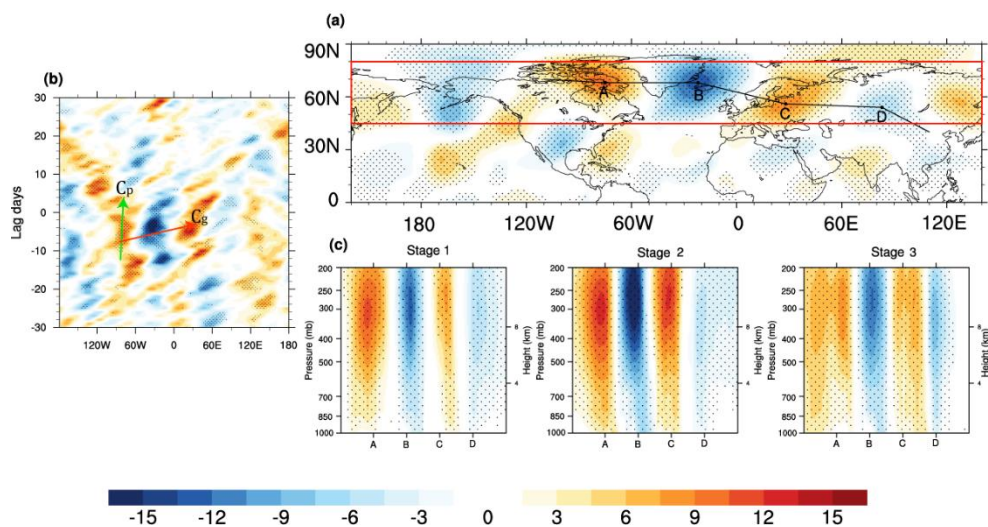
234
 235 **Fig.3 a-c** Lead-lag composite of anomalous SAT (shading; unit: K) and 500-hPa geopotential height
 236 (contour; unit: gpm, CI = 60gpm) fields for the three type cold events from lag -12 to 6 days. The green
 237 box indicates the study area where the cold event occurs. The thick line and shaded area denote that the
 238 anomaly is statistically significant above the 95% level of confidence

239 **4 The formation mechanisms of the three types of wave trains**

240 In this section, the period of cold events is further divided into three stages, that is, stage 1: averaged
 241 in lag -14 to -8 days, which represents the time that initial atmospheric signal begins; stage2: averaged
 242 in lag -7 to -1 days, which on behalf of the development stage of atmospheric anomalies; stage 3:
 243 averaged in lag 0 to 6 days, indicating the occurrence of the cold event. In the following, we will discuss
 244 the formation mechanisms of three types of cold events separately.

245 **4.1 type1: Baffin Bay-origin**

246 In general, the Rossby waves can be referred to by deviations from the zonal flow, which are usually
 247 diagnosed by the meridional wind of upper-troposphere that can intuitively present the properties of
 248 RWPs (Wirth et al. 2018). The group and phase velocity of RWPs can also be reflected on the Hovmoller
 249 diagram of meridional wind, which can detect downstream development as a tool(Persson 2017). Fig.4
 250 captures the structure of v' in horizontal, vertical and its Hovmoller diagram. In the mean v' fields of
 251 three stages at 250-hPa (Fig.4a), two columns of distinct RWPs can be seen at the Aleutian Islands to the
 252 northern Florida Peninsula (170°W-60°W) and the Baffin Bay to northern Asia (30°W-140°E).
 253 Apparently, it is the one near the east (30°W-140°E) that cause the cold anomaly of Eurasia. Therefore,
 254 the Hovmoller diagram of the latitude band of this column RWPs (red box in Fig.4a) is shown in Fig.4b.
 255 It can be seen that the first RWP generated at 60°W around lag -20 days and began to develop downstream.
 256 At lag -10 days, a situation of larger group velocity than phase velocity can be identified, as shown by
 257 the marked arrow (Fig.4b), which signifies a rapid downstream propagation of energy, resulting in the
 258 cold event that occurred at lag 0 days. Then, the RWPs dissipate around lag 6 days, along with the
 259 termination of the cold event. Furthermore, Fig 4c presents the vertical structure of four RWPs centers
 260 labeled in Fig.4a at three stages. The strongest amplitude mainly shows in the upper troposphere,
 261 consistent with the previous study (Krishnamurti et al. 1977). In addition, it is worth noting that the
 262 RWPs reach the maximum amplitude at stage 2 rather than stage 3, i.e., before the outbreak of cold event,
 263 which indicates that extreme weather may be just around the corner when the strong amplitude RWPs
 264 signal emerges. In other words, it validates the role of downstream development of RWPs for cold events
 265 (Chang and Yu 1999; Glatt et al. 2011).

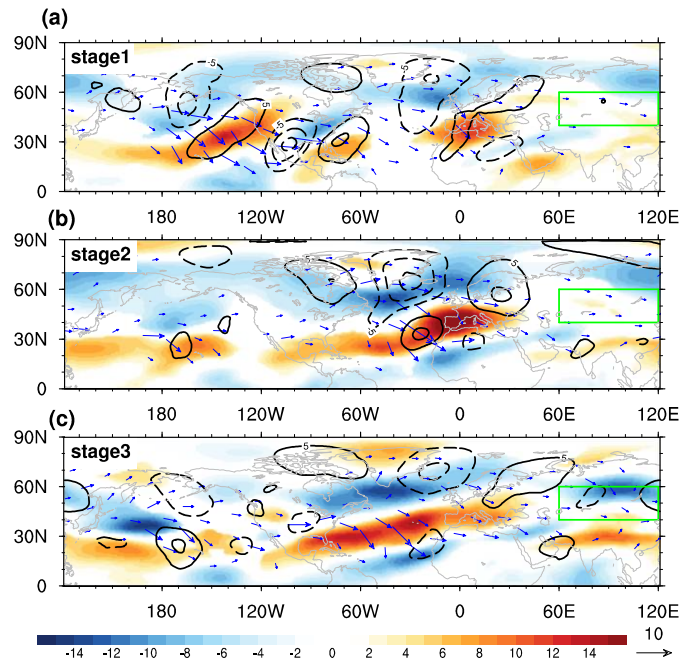


266
 267

268 **Fig.4 a** The field of 250-hPa anomalous meridional wind (v') (unit: m s^{-1}) averaged in three stages. **b**
 269 Composite Hovmoller diagram of the 250-hPa v' averaged in 45-80°N (red box in **a**). **c** Vertical section
 270 of v' in three stages along the line as indicated in **a**. Dotted areas denote significant differences exceeding
 271 95% confidence level

272 To learn more about the development process of the RWPs, Fig. 5 shows the anomalous distribution
 273 of meridional and zonal winds and T-N wave activity flux in the upper troposphere. It shows there are
 274 two columns of RWPs in stage 1 (Fig.5a), as mentioned above. In stage 2 (Fig.5b), however, the western
 275 side of RWPs in the Pacific disappears, and the WAF transported from eastern Greenland to downstream
 276 reinforces in the Atlantic. Meanwhile, the negative westerly anomalies in the mid-Atlantic to Norwegian
 277 sea intensify, which are conducive to the progress of the Rossby wave (Francis and Vavrus 2012), thus
 278 the RWPs on the eastern side strengthen and develop. Afterward, the WAF transmits to Eurasia in stage
 279 3, leading to the beginning of the cold event.

280 In general, it is known that the westerly momentum plays a crucial dynamic role in the development
 281 and propagation of the Rossby wave (Takaya and Nakamura 2001; Wirth et al. 2016). But what causes
 282 the disturbance of this wave train? Next, we will examine the formation mechanism for these RWPs at
 283 Baffin Bay area, where the first wave packet is situated.

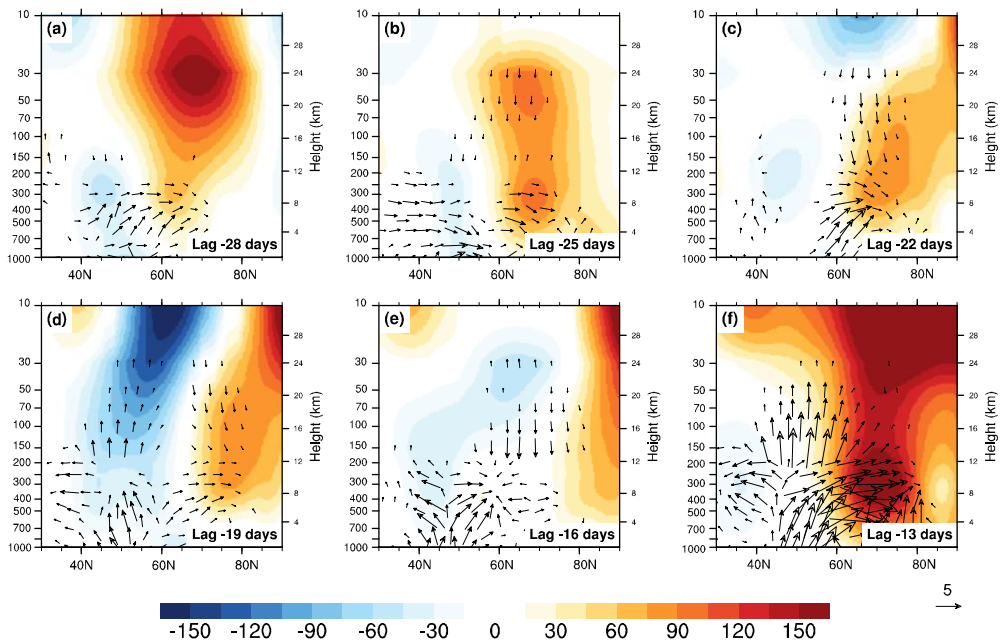


284

285 **Fig. 5** Averaged composite fields of anomalous meridional wind (contour, unit: m s^{-1}) and zonal winds
 286 (shading, unit: m s^{-1}) and T-N wave flux (vector, unit: $\text{m}^2 \text{s}^{-2}$) at 200-hPa in **a** stage 1, **b** stage 2, **c** stage

287 3 based on type 1 event. The green box indicates the area where the cold event occurs. The Shading area
 288 and contour denote significant differences exceeding 95% confidence level

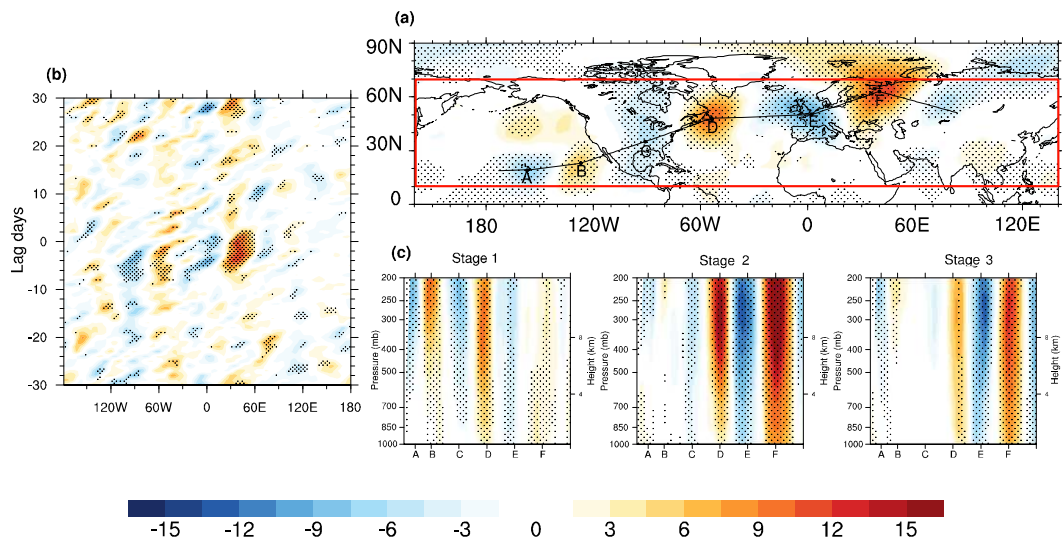
289 To examine the driving source of the disturbance, the time-evolution fields of meridional averaged
 290 of vertical WAF, and geopotential height anomalies over the Baffin Bay area (30°W-90°W) before stage
 291 1 are illustrated in Fig. 6. It shows that there is a positive center of anomaly that appears in the upper
 292 stratosphere at lag -28 days (Fig.6a), after which it begins to fall (Fig.6b), along with a downward
 293 propagating WAF in the middle stratosphere until lag -16 days (Figs.6b-e), corresponding to the initial
 294 period of the RWP over Baffin Bay emerging in Fig.4b. In this way, the initial disturbances in Baffin Bay
 295 are thus concluded by the downward spread of energy in the stratosphere. In addition, it is worth
 296 mentioning that there is an upward and northward propagation of WAF from 50°N-60°N at lag -16 to -
 297 13 days (Figs.6e-f), which exactly corresponds to the end position of the western RWPs over eastern-
 298 North Pacific that appeared in Fig.6a. Therefore, we suppose that the western RWPs in Fig.6a may also
 299 contribute some energy to the eastern RWPs, which explains why it disappears immediately in stage 2
 300 (Fig.6b). Martius et al. (2010) also proposed that if multiple waveguides are close to each other, the
 301 RWPs may transfer from one waveguide to another.



302
 303 **Fig.6 a-f** Lead-lag composites of 30°W-90°W averaged cross section of geopotential height anomalies
 304 (shading; unit: gpm) and WAF (vectors; units: for horizontal component $m^2 s^{-2}$; for vertical component
 305 $10^{-2} Pa m s^{-2}$) based on type 1 event. The shading area indicates the anomalies of geopotential height
 306 exceeding 95% confidence level

307 **4.2 type2: Pacific-origin**

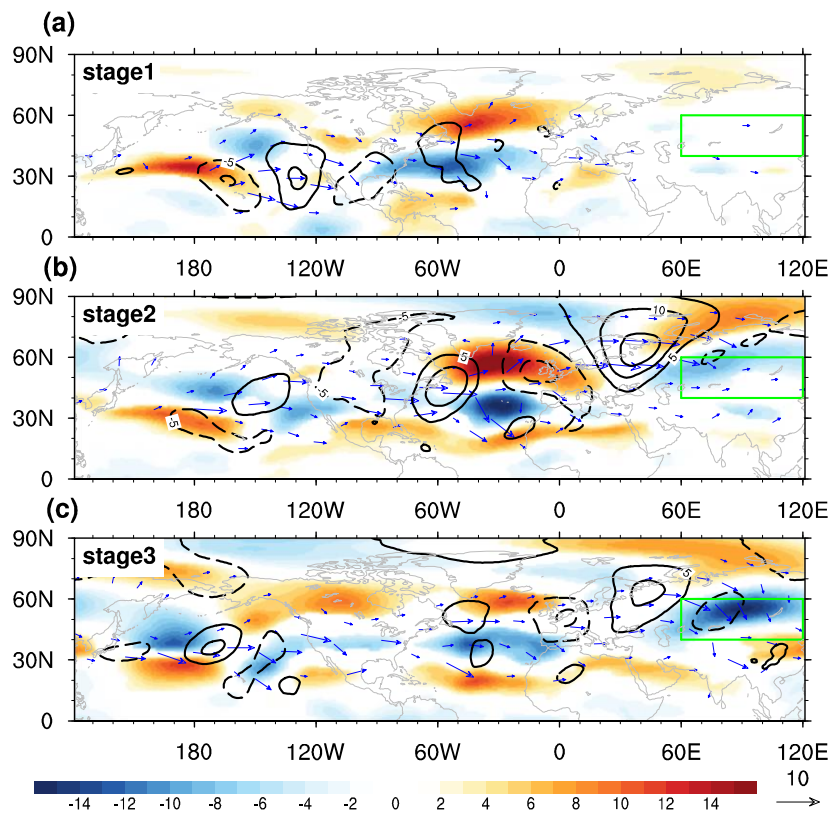
308 For type 2 event, a similar analysis method is applied. As shown in Fig.7a, a column of RWPs begins
 309 from Hawaii Islands and extends to Europe. The Hovmoller diagram of latitude band of this wave train
 310 shown in Fig.7b exhibits that the RWPs begin to propagate eastward at about lag -9 days, with the same
 311 situation of faster group velocity as type 1, but with a shorter growth cycle. In Fig.7c, which presents
 312 three stages of vertical v' of the RWPs, apparent downstream development structure can be recognized:
 313 in stage 1, four weak RWP centers (A-D points) emerge in the upper troposphere; then, new RWPs appear
 314 downstream and reach maximum amplitude in stage 2 (D-F points), while the upstream wave packets
 315 recede quickly; in stage 3, similar with type 1 event, the cooling occurs and RWPs further fade away.
 316 Anyway, we know from the above analysis that these RWPs have different features and structures from
 317 type 1. Next, we will further investigate the formation mechanism of this wave train.



318
 319 **Fig.7** Same as in Fig.4 but for type 2 event

320 Fig. 8 presents the anomalous distribution of meridional and zonal winds and WAF at the upper
 321 troposphere. In stage 1(Fig.8a), a distinct wave train appears from the central North Pacific to the western
 322 Atlantic; simultaneously, positive westerly anomalies in the central Pacific and negative westerly
 323 anomalies in the southern side of the Gulf of Alaska are observed. Furthermore, the configuration of
 324 upper-level divergence and lower-level convergence dominated the central Pacific (not shown). That is
 325 to say, in the middle of the North Pacific, where the outlet of the westerly jet is located, cyclonic shear
 326 and up-flow exist, which is conducive to the generation of cyclonic disturbance. Therefore, we speculate
 327 that the formation of these RWPs results from the increase of cyclonic shear over the outlet area of the

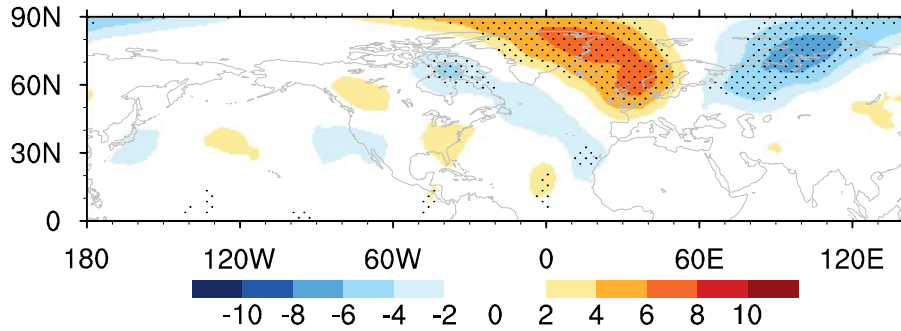
328 westerly jet. Meanwhile, the westerly anomalies over North Atlantic are northerly, and enhance at stage
 329 2 (Fig.8b), which may serve as a waveguide that further prompts the development of upstream wave
 330 packets to the European continent. It can also be seen from the evolution of WAF that the arrows follow
 331 the northerly westerlies towards Europe. In stage 3 (Fig.8c), the RWPs in the upstream vanish, and the
 332 downstream RWPs develop to the cold event area. The previous study has pointed out that the RWPs in
 333 the North Pacific often seed new wave packets over the North Atlantic for it inclined to deviate from the
 334 zonal direction and propagate equatorward into the subtropics (Wirth et al. 2018). In our case, though,
 335 the northerly westerly anomalies over the Atlantic relay the wave train develop to the northern Eurasian
 336 continent rather than southward.



337
 338 **Fig.8** Same as in Fig.5 but based on the type 2 event

339 **4.3 type 3: Atlantic-origin**

340 As shown in Fig.9, unlike the first two types of events, the averaged field of v' of type 3 event
 341 presents a dipole structure over the Greenland Sea and the Kara Sea, no prominent RWPs system that
 342 extended from upstream. Therefore, we speculate that this type of cold event may be related to some
 343 local development mechanism rather than the downstream development of remote RWPs like the first
 344 two types of events.

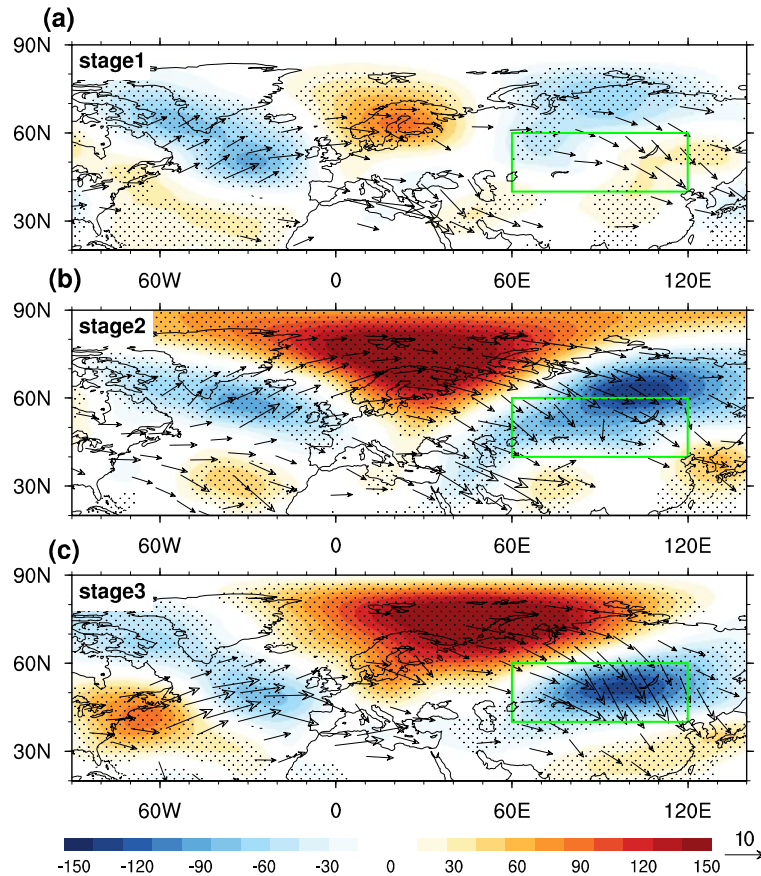


345

346 **Fig.9** The averaged field of 250-hPa anomalous meridional wind (v') in three stages of type 3 cold event.

347 Dotted areas denote significant differences exceeding 95% confidence level

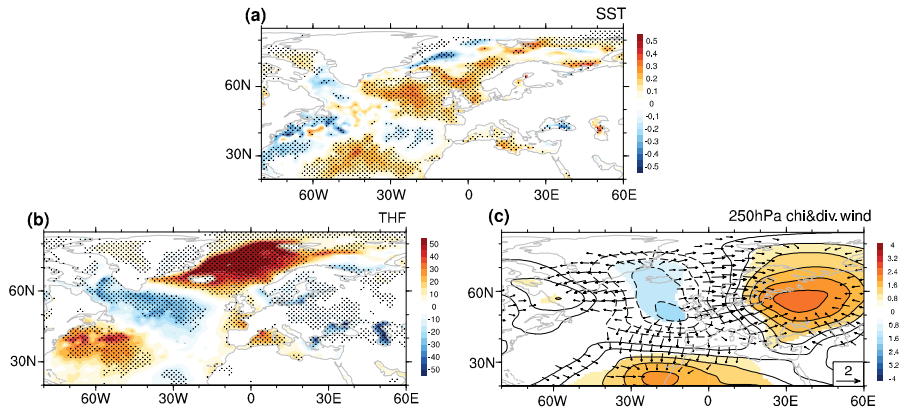
348 To further understand its evolution process, the anomalous geopotential height and WAF fields in
 349 the upper troposphere are given in Fig.10. It is shown that there is an anticyclone anomaly over
 350 Scandinavia with two other opposite signs over the Atlantic and Northern Russia at stage 1; meanwhile,
 351 the northeastward WAF originated from the middle of the Atlantic can be observed. Afterward, the
 352 anticyclone anomalies develop to the strongest amplitude, along with enhanced WAF transport to the
 353 downstream, resulting in the cooling over Eurasia in stage 3. Overall, this atmospheric system resembles
 354 the teleconnection mode of the SCAND pattern, which may cause strong climate anomalies in the Arctic
 355 and Eurasia (Wang and Tan 2020). There are various reasons that can lead to the formation of SCAND
 356 patterns, such as the vorticity source over Western Europe (Liu et al. 2014), the Atlantic convective
 357 heating or the height disturbance over the Arctic (Wang and Tan 2020), and the feedback forcing from
 358 high-frequency eddies along the Atlantic storm track (Bueh and Nakamura 2007).



359

360 **Fig.10** Averaged composite fields of 250-hPa geopotential height anomalies (shading; unit: gpm) and
 361 WAF (vectors; unit: $\text{m}^2 \text{s}^{-2}$) of **a** stage 1, **b** stage 2, **c** stage 3 based on type 3 event. Dotted areas denote
 362 significant differences of the anomalies of geopotential height exceeding 95% confidence level

363 To confirm the influential role of the Atlantic, Fig.11 examines the anomaly of sea surface
 364 temperature, turbulent heat flux, and potential velocity and divergent wind in the upper troposphere
 365 averaged of stages 1-2 over mid-North Atlantic. The warm SST anomalies can be observed over the
 366 central Atlantic (Fig.11a); furthermore, the upward turbulent flux anomalies (negative area) showing up
 367 in the warm water area (Fig.11b), indicating that the force of SST to atmosphere exists; Meanwhile, the
 368 anomalous lower-tropospheric convergence (omitted) and upper-tropospheric divergence present over
 369 the warm SST region (Fig.11c). Therefore, the wave train may be excited by the sea-air interaction
 370 process due to the warm SST anomalies over the North Atlantic. The result is different from Liu et al.
 371 (2014), who pointed out that the upper-tropospheric divergent flow induced by the Indian Ocean heating
 372 could lead to divergence anomalies over the Mediterranean and subsequently motivate the formation of
 373 the SCAND pattern. In our work, the divergence flow is related to the warm SST over the Atlantic.



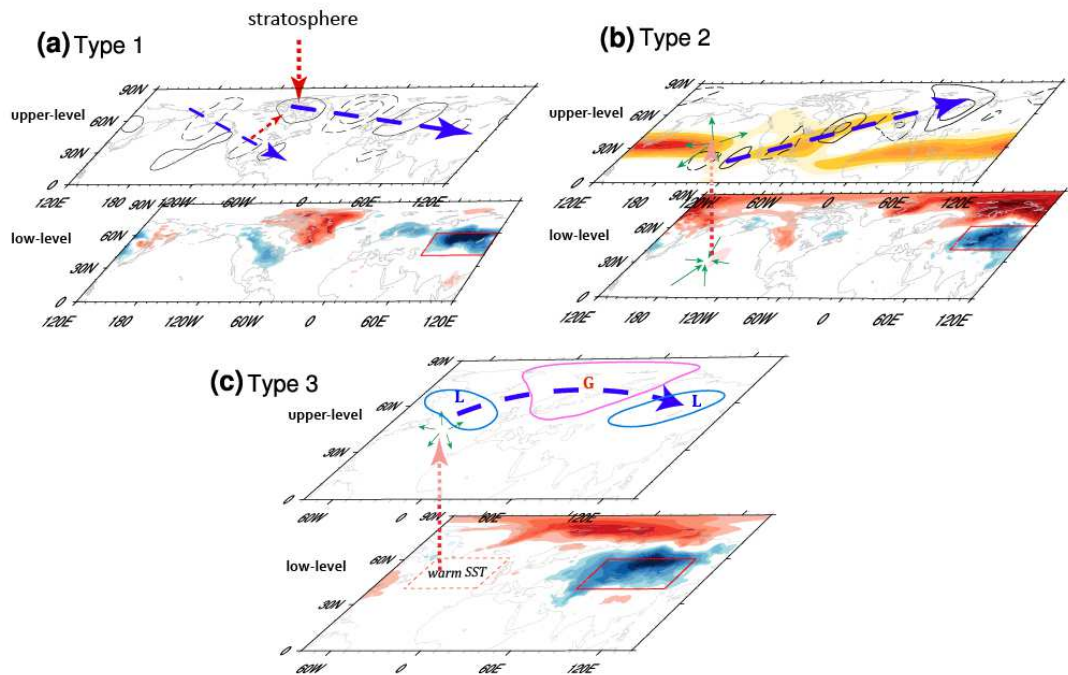
374

375 **Fig.11** The averaged anomalous field of **a** SST (unit: K) **b** THF (unit: $W m^{-2}$) **c** 250-hPa velocity
 376 potential (unit: $1 \times 10^6 m^2 s^{-1}$) and divergent wind (unit: $m s^{-1}$) based on stage1-2 of type 3 event. Dotted
 377 areas in **a-b** and shading area and vectors in **c** denote significant differences exceeding 95% confidence
 378 level

379 5 Summary and discussions

380 In this work, we categorize the extreme cold events over central Eurasia into three groups from the
 381 perspective of precursory atmospheric disturbance. According to the classification, each category of the
 382 anomalous atmospheric modes is found to be associated with Rossby wave trains originating from
 383 different positions. Fig.12 presents the atmospheric disturbance origin and development path of three
 384 types of events. For type 1 (Fig.12a), two branches of RWPs can be clearly seen. It is the one located at
 385 the Baffin Bay to Europe continent that affects the cooling over Eurasia, which is generated by the
 386 stratospheric downwards energy over the Baffin Bay; besides, the one on the left side may also play a
 387 role. When the RWPs propagate eastward, with group velocity larger than phase velocity, they reach
 388 maximum amplitude prior to the advent of cold event, which may serve as a precursor signal of cooling
 389 eruption. For type 2 (Fig.12b), the westerlies play a crucial role. Firstly, the disturbance generates at the
 390 exit of the westerly jet over the North Pacific, where cyclone shear exists, then propagates downstream
 391 as wave packets; after that, the northerly westerlies over North Atlantic extend the wave train to the
 392 Eurasian continent, with the same downstream development situation like type1, leading to the outbreak
 393 of extreme cooling. In many studies, the RWPs are usually found in the subtropical westerly jet over Asia
 394 (Watanabe 2004), which can easily affect the precipitation over south China (Li and Sun 2015; Hu et al.
 395 2018; Sun and Guan 2020). In this work, however, the westerlies over North Atlantic can also act as a
 396 waveguide. For type 3 (Fig.12c), the SCAND-like mode presents over the Atlantic to Europe, but no

397 prominent RWPs system appears upstream like the first two types. It is concluded that the wave train of
 398 this type may be triggered by the process of sea-air interaction over the mid-North Atlantic.



399
 400 **Fig.12** Schematic diagram for three types of events showing the development source and propagation
 401 path of Rossby wave packets in stage 1-2 (upper-level) and their effect on the surface temperature in
 402 stage 3 (low-level) of **a** type 1, **b** type 2, **c** type 3 event. In the upper-level, the contour in **a** and **b** indicate
 403 the meridional wind anomalies, the contour in **c** denote the geopotential height anomalies, and the yellow
 404 shading area in **b** indicates the zonal wind; the blue dash arrows signify the development direction of the
 405 wave train, and the red dash arrows in **a** denote the direction of energy transfer. In the low-level, the
 406 shading area represents the anomalies of surface air temperature on stage 3 (blue denote negative anomaly,
 407 red denote positive anomaly)

408 As discussed in Wirth et al. (2018), there is no clear answer yet whether the presence of precursor
 409 RWPs helps to improve the prediction of the extreme weather, which hinges on the systematic contacts
 410 between RWPs and extreme weather. In our work, the first two types of events possess apparently RWPs
 411 signals about 10 days before the occurrence of extreme cooling but not the third event, which verifies
 412 the uncertainty of the link between extreme weather and precursor RWPs, but also suggests that the
 413 RWPs can indeed act as a precursor signal of extreme cooling to some extent. In other words, the results
 414 have some indicative implications for the improvement of weather extended forecast. Certainly, it is not
 415 enough to illuminate the connection from a small sample of extreme cases we selected, thus more

416 possible mechanisms of precursory wave trains that can lead to extreme weather remains to be explored
417 in the future.

418 In addition, since we divide the cold events based on the atmospheric circulation, some external
419 force factors that may also relate to Eurasia cooling, such as the warming of the Arctic (Cohen 2016; Ma
420 et al. 2018, Mori et al. 2019), are not presenting distinctly in our cases due to the composite analysis.
421 Consequently, further studies that probe into various outside factors on the Rossby wave train that lead
422 to extreme cooling deserve to be explored.

423

424

425

426

427

428

429

430

431

432

433

434

435

436

437

438

439

440

441

442 **Acknowledgements**

443 This work was supported by the National Key Scientific Research Program of China (2019YFA0607004),
444 the National Science Foundation of China (42075024) and Shandong Natural Science Foundation Project
445 (ZR2019ZD12).

446 **Reference**

- 447 Barton Y, Giannakaki P, von Waldow H, Chevalier C, Pfahl S, Martius O (2016) Clustering of
448 regional-scale extreme precipitation events in southern Switzerland. *Mon Wea Rev* 144(1): 347–
449 369. <https://doi.org/10.1175/MWR-D-15-0205.1>
- 450 Barnston AG, and Livezey RE (1987) Classification, seasonality and persistence of low-frequency
451 atmospheric circulation patterns. *Mon Wea Rev* 115:1083–1126. [https://doi.org/10.1175/1520-
452 0493\(1987\)115.1083:CSAPOL.2.0.CO;2](https://doi.org/10.1175/1520-0493(1987)115.1083:CSAPOL.2.0.CO;2)
- 453 Bosart LF, Moore BJ, Cordeira JM, Archambault H M (2017) Interactions of North Pacific tropical,
454 midlatitude, and polar disturbances resulting in linked extreme weather events over North
455 America in October 2007. *Mon Wea Rev* 145:1245– 1273. [https://doi.org/10.1175/MWR-D-16-
456 0230.1](https://doi.org/10.1175/MWR-D-16-0230.1)
- 457 Bueh C, Nakamura H (2007) Scandinavian pattern and its climatic impact. *Q J Roy Meteor Soc* 133:
458 2117–2131. <https://doi.org/10.1002/qj.173>
- 459 Branstator, G (2002) Circumglobal teleconnections, the jet stream waveguide, and the North Atlantic
460 Oscillation. *J Clim* 15(14), 1893–1910. [https://doi.org/10.1175/1520-
461 0442\(2002\)015h1893:CTTJSWi2.0.CO;2](https://doi.org/10.1175/1520-0442(2002)015h1893:CTTJSWi2.0.CO;2)
- 462 Casado MJ, Pastor MA, Doblas-Reyes FJ (2009) Euro-Atlantic circulation types and modes of
463 variability in winter. *Theor Appl Climatol* 96:17–29. <https://doi.org/10.1007/s00704-008-0036-2>
- 464 Chang, and Yu DB, (1999) Characteristics of wave packets in the upper troposphere Part I: Northern
465 Hemisphere winter. *J Atmos Sci* 56:1708–1728. [https://doi.org/10.1175/1520-
466 0469\(1999\)056.1708: COWPIT.2.0.CO;2](https://doi.org/10.1175/1520-0469(1999)056.1708: COWPIT.2.0.CO;2)
- 467 Chen S, Wu R, Chen W, Hu K, Yu B (2020) Structure and dynamics of a springtime atmospheric wave
468 train over the North Atlantic and Eurasia. *J Clim* 54(11–12): 5111–5126.
469 <https://doi.org/10.1007/s00382-020-05274-7>
- 470 Cohen JL, Furtado JC, Barlow M, Alexeev VA, Cherry JE (2012) Asymmetric seasonal temperature
471 trends. *Geophys Res Lett*, 39(4): 1–7. <https://doi.org/10.1029/2011GL050582>
- 472 Cohen J, Screen J, Furtado J et al (2014) Recent Arctic amplification and extreme mid-latitude
473 weather. *Nature Geosci* 7:627–637. <https://doi.org/10.1038/ngeo2234>
- 474 Cohen J. (2016) An observational analysis: Tropical relative to Arctic influence on midlatitude weather
475 in the era of Arctic amplification. *Geophys Res Lett* 6: 1–402.
476 <https://doi.org/10.1002/2016GL069102>

477 Cohen J, Zhang X, Francis J et al (2020) Divergent consensus on Arctic amplification influence on
478 midlatitude severe winter weather. *Nat Clim Change* 10:20–29. [https://doi.org/10.1038/s41558-](https://doi.org/10.1038/s41558-019-0662-y)
479 [019-0662-y](https://doi.org/10.1038/s41558-019-0662-y)

480 Dee DP et al (2011) The ERA-Interim reanalysis: configuration and performance of the data
481 assimilation system. *Q J R Meteorol Soc* 137:553–597. <https://doi.org/10.1002/qj.828>

482 Francis JA, Vavrus SJ (2012) Evidence linking Arctic amplification to extreme weather in
483 midlatitudes. *Geophys Res Lett* 39:L06801. <http://dxdoi.org/10.1029/2012GL051000>

484 Fragkoulidis G, Wirth V, Bossmann P, Fink AH (2018) Linking Northern Hemisphere temperature
485 extremes to Rossby wave packets. *Q J Roy Meteor Soc* 144(711):553–566.
486 <https://doi.org/10.1002/qj.3228>

487 Grazzini F, Fragkoulidis G, Teubler F, Wirth V, Craig GC (2021) Extreme precipitation events over
488 northern Italy. Part II: Dynamical precursors. *Q J R Meteorol Soc* 147:1237– 1257.
489 <https://doi.org/10.1002/qj.3969>

490 Gong Z, Feng G, Ren F, Li, J (2014) A regional extreme low temperature event and its main
491 atmospheric contributing factors. *Theor Appl Climatol* 117(1):195–206.
492 <https://doi.org/10.1007/s00704-013-0997-7>

493 Glatt I, Dörnbrack A, Jones S, Keller J, Martius O, Müller A, Peters DHW, Wirth V (2011) Utility of
494 Hovmöller diagrams to diagnose Rossby wave trains. *Tellus A* 63(5):991–1006.
495 <https://doi.org/10.1111/j.1600-0870.2011.00541.x>

496 Horton DE, Johnson NC, Singh D, Swain DL, Rajaratnam B, Diffenbaugh NS (2015) Contribution of
497 changes in atmospheric circulation patterns to extreme temperature trends. *Nature*
498 522(7557):465–469. <https://doi.org/10.1038/nature14550>

499 Hu K, Huang G, Wu R, Wang L (2018) Structure and dynamics of a wave train along the wintertime
500 Asian jet and its impact on East Asian climate. *Clim Dyn* 51(11–12):4123–4137.
501 <https://doi.org/10.1007/s00382-017-3674-1>

502 Hoskins BJ, Ambrizzi T (1993) Rossby wave propagation on a realistic longitudinally varying flow. *J*
503 *Atmos Sci* 50:1661–1671. [https://doi.org/10.1175/1520-0469\(1993\)050,1661:RWPOAR.2.0.CO;2](https://doi.org/10.1175/1520-0469(1993)050<1661:RWPOAR.2.0.CO;2)

504 Kretschmer M, Cohen J, Matthias V, Runge J, Coumou D (2018). The different stratospheric influence
505 on cold-extremes in Eurasia and North America. *Npj Clim Atmos Sci* 1(1):1–10.
506 <https://doi.org/10.1038/s41612-018-0054-4>

507 Krishnamurti TN, Molinari J, Pan H, and Wong V (1977) Downstream amplification and formation of
508 monsoon disturbances. *Mon Wea Rev* 105:1281–1297. [https://doi.org/10.1175/1520-](https://doi.org/10.1175/1520-0493(1977)105<1281:DAAFOM>2.0.CO;2)
509 [0493\(1977\)105<1281:DAAFOM>2.0.CO;2](https://doi.org/10.1175/1520-0493(1977)105<1281:DAAFOM>2.0.CO;2)

- 510 Kosaka Y, Nakamura H, Watanabe M, Kimoto M (2009) Analysis on the dynamics of a wave-like
511 teleconnection pattern along the summertime Asian jet based on a reanalysis dataset and climate
512 model simulations. *J Meteor Soc Jpn* 87(3):561–580. <https://doi.org/10.2151/jmsj.87.561>
- 513 Kug JS, Jeong JH, Jang YS, Kim BM, Folland CK, Min SK, Son SW (2015). Two distinct influences
514 of Arctic warming on cold winters over North America and East Asia. *Nat Geosci* 8(10):759–
515 762. <https://doi.org/10.1038/ngeo2517>
- 516 Kim KY, Son SW (2016) Physical characteristics of Eurasian winter temperature variability. *Environ*
517 *Res Lett* 11(4):044009. <https://doi.org/10.1088/1748-9326/11/4/044009>
- 518 Li C, Sun J (2015) Role of the subtropical westerly jet waveguide in a southern China heavy rainstorm
519 in December 2013. *Adv Atmos Sci* 32(5):601–612. <https://doi.org/10.1007/s00376-014-4099-y>
- 520 Liu Y, Wang L, Zhou W, Chen W (2014) Three Eurasian teleconnection patterns: Spatial structures,
521 temporal variability, and associated winter climate anomalies. *Clim Dyn* 42(11–12):2817–2839.
522 <https://doi.org/10.1007/s00382-014-2163-z>
- 523 Lu C, Xie S, Qin Y, Zhou J (2016) Recent Intensified Winter Coldness in the Mid-High Latitudes of
524 Eurasia and Its Relationship with Daily Extreme Low Temperature Variability. *Adv Meteorol*
525 2016:17–19. <https://doi.org/10.1155/2016/3679291>
- 526 Luo D, Xiao Y, Yao Y, et al (2016) Impact of ural blocking on winter warm Arctic-cold Eurasian
527 anomalies. Part I: Blocking-induced amplification. *J Clim* 29:3925–3947.
528 <https://doi.org/10.1175/JCLI-D-15-0611.1>
- 529 Luo D, Xiao Y, Diao Y, et al (2016) Impact of Ural blocking on winter warm Arctic-cold Eurasian
530 anomalies. Part II: The link to the North Atlantic Oscillation. *J Clim* 29:3949–3971.
531 <https://doi.org/10.1175/JCLI-D-15-0612.1>
- 532 Luo B, Wu L, Luo D, Dai A, Simmonds I (2019) The winter midlatitude-Arctic interaction: effects of
533 North Atlantic SST and high-latitude blocking on Arctic sea ice and Eurasian cooling. *Clim Dyn*
534 52(5–6):2981–3004. <https://doi.org/10.1007/s00382-018-4301-5>
- 535 Martius O, Schwierz C, Davies HC (2010) Tropopause-level waveguide. *J Atmos Sci* 67(3):866–879.
536 <https://doi.org/10.1175/2009JAS2995.1>
- 537 Ma S, Zhu C, Liu B, Zhou T, Ding Y, Orsolini YJ (2018) Polarized response of East Asian winter
538 temperature extremes in the Era of arctic warming. *J Clim* 31(14):5543–5557.
539 <https://doi.org/10.1175/JCLI-D-17-0463.1>
- 540 Mori M, Kosaka Y, Watanabe M, Nakamura H, Kimoto M (2019) A reconciled estimate of the
541 influence of Arctic sea-ice loss on recent Eurasian cooling. *Nat Clim Change* 9(2):123–129.
542 <https://doi.org/10.1038/s41558-018-0379-3>

- 543 Overland JE, Wang MY (2010) Large-scale atmospheric circulation changes are associated with the
544 recent loss of Arctic sea ice. *Tellus A* 62(1):1-9. <https://doi.org/10.1111/j.1600-0870.2009.00421.x>
545
- 546 Persson A (2017) The story of the Hovmöller diagram—An (almost) eyewitness account. *Bull Amer*
547 *Meteor Soc* 98:949–957. <https://doi.org/10.1175/BAMS-D-15-00234.1>
- 548 Sato K, Inoue J, Watanabe M (2014) Influence of the Gulf Stream on the Barents Sea ice retreat and
549 Eurasian coldness during early winter. *Environ Res Lett* 9(8):84009.
550 <https://doi.org/10.1088/1748-9326/9/8/084009>
- 551 Sun S, Guan, Z (2020) Rossby wave packets in the upper troposphere and their associations with
552 climatological summertime daily precipitation in MLRYR of China. *Atmos Sci Lett* 1–9.
553 <https://doi.org/10.1002/asl.1023>
- 554 Shi N, Bueh C, Ji LR, Wang PX (2009) The impact of mid- and high-latitude Rossby wave activities
555 on the medium-range evolution of the EAP pattern during the pre-rainy period of South China.
556 *Acta Meteorologica Sinica* 23(3):300–314. [https://doi.org/10.1016/S1003-6326\(09\)60084-4](https://doi.org/10.1016/S1003-6326(09)60084-4)
- 557 Shi J, Wu K, Qian W, et al (2021) Characteristics, trend, and precursors of extreme cold events in
558 northwestern North America. *Atmos Res* 249:105338.
559 <https://doi.org/10.1016/j.atmosres.2020.105338>
- 560 Takaya K, Nakamura H (2001) A formulation of a phase-independent wave-activity flux for stationary
561 and migratory quasi geostrophic eddies on a zonally varying basic flow. *J Atmos Sci* 58:608–627
- 562 Wallace JM, Gutzler DS (1981) Teleconnections in the geopotential height field during the Northern
563 Hemisphere winter. *Mon Wea Rev* 109:784–812. [https://doi.org/10.1175/1520-0493\(1981\)109<0784:TITGHF>2.0.CO;2](https://doi.org/10.1175/1520-0493(1981)109<0784:TITGHF>2.0.CO;2)
564
- 565 Watanabe M (2004) Asian jet waveguide and a downstream extension of the North Atlantic oscillation.
566 *J Clim* 17:4674–4691. [https://doi.org/10.1175/1520-0469\(1993\)050<2038:DDOBWA>2.0.CO;2](https://doi.org/10.1175/1520-0469(1993)050<2038:DDOBWA>2.0.CO;2)
- 567 Wang M, Tan B (2020) Two types of the Scandinavian pattern: Their formation mechanisms and
568 climate impacts. *J Clim* 33(7):2645–2661. <https://doi.org/10.1175/JCLI-D-19-0447.1>
- 569 Wirth V, Eichhorn J (2014) Long-lived Rossby wave trains as precursors to strong winter cyclones
570 over Europe. *Q J Roy Meteor Soc* 140(680):729–737. <https://doi.org/10.1002/qj.2191>
- 571 Wirth V, Riemer M, Chang EKM, Martius O (2018) Rossby wave packets on the midlatitude waveguide-
572 A review. *Mon Wea Rev* 146(7):1965–2001. <https://doi.org/10.1175/MWR-D-16-0483.1>
- 573 Wu B, Yang K, Francis JAA (2017) Cold Event in Asia during January–February 2012 and Its Possible
574 Association with Arctic Sea Ice Loss. *J Clim* 30(19):7971–7990.

- 575 Zhang X, Lu C, Guan Z (2012) Weakened cyclones, intensified anticyclones and recent extreme cold
576 winter weather events in Eurasia. *Environ Res Lett* 7(4): 044044. [https://doi.org/101088/1748-](https://doi.org/101088/1748-9326/7/4/044044)
577 [9326/7/4/044044](https://doi.org/101088/1748-9326/7/4/044044)
- 578 Zheng Fei, Yuan Y, Ding YH, Li Kexin et al. (2021). The 2020/21 Extremely Cold Winter in China
579 Influenced by the Synergistic Effect of La Niña and Warm Arctic. *Advances in Atmospheric*
580 *Sciences*. 10.1007/s00376-021-1033-y.
- 581 Zhuo WQ, and Jiang ZN (2020) Possible links between Arctic sea ice loss and Eurasian cold winter
582 events. *J Meteor Res* 34(6):1214–1225. <https://doi.org/10.1007/s13351-020-0052-4.1>

Supplementary Files

This is a list of supplementary files associated with this preprint. Click to download.

- [SupplementaryInformation.pdf](#)